Journal of Solid State Chemistry **148,** 108–118 (1999)
Article ID jssc.1999.8385, available online at http://www.idealibrary.com on IDEAL®

A Strontium-Rich 2201-Type Cobaltite with a Nonmodulated Structure: $Bi_{1-x}Sr_{3+x}CoO_{6-\delta}$

D. Pelloquin, A. C. Masset, A. Maignan, M. Hervieu, C. Michel, and B. Raveau

Laboratoire CRISMAT, UMR 6508 associée au CNRS, ISMRA et Université de Caen, 6, Boulevard du Maréchal Juin, 14050 Caen Cedex, France

Received January 26, 1999; in revised form April 27, 1999; accepted May 21, 1999

DEDICATED TO C. N. R. RAO FOR HIS 65TH BIRTHDAY

A strontium-rich 2201-type oxide, $Bi_{1-x}Sr_{3+x}CoO_{6-\delta}$, with a nonmodulated structure has been synthesized. X-ray powder diffraction and high-resolution electron microscopy show a 1:1 ordering of Bi^{3+} and Sr^{2+} species within the two intermediate $[Bi_{0.5}Sr_{0.5}O]_\infty$ layers. The distorted $[CoO_2]_\infty$ layers can also be described as built up from CoO_6 octahedra and CoO_5 pyramids, stacked along a alternately. In this structure, Bi^{3+} exhibits a tetrahedral coordination BiO_3L, taking into consideration its $6s^2$ lone pair denoted *L*. The magnetic behavior of this trivalent cobalt oxide suggests that this species is not purely high spin and shows an antiferromagnetic transition below 50 K, similar to that observed in the tubular cobaltite. © 1999 Academic Press

INTRODUCTION

The discovery of Bi-based superconductors $Bi_2Sr_2Ca_{n-1}Cu_nO_{2n+4+\delta}$ (see for a review Refs. (1, 2)) has opened the route to research of other transition metal oxides with similar structure, involving iron, manganese, or cobalt. This is the case for the 2201-type oxides $BiPbSr_2FeO_{6+\delta}$ (3), $Bi_2Sr_2MnO_{6+\delta}$ (4), and $Bi_2Sr_2CoO_{6+\delta}$ (3), which are isotypic to the 22-K-superconductor $Bi_2Sr_2CuO_{6+\delta}$ (5). These bidimensional oxides differ from the corresponding cuprate by their magnetic properties which similar to superconductivity are likely to be influenced by the strongly modulated character of the structure (the modulation vector is parallel to **b**). These 2201 oxides indeed exhibit undulating bismuth oxygen layers, characterized by an inhomogeneous distribution of Bi^{3+} cations, with a fluctuation of the Bi–Bi distances, leading to the formation of concentrated and deficient bismuth zones alternatively (6). Moreover, the nature of the modulation varies with the transition element, so that an incommensurate superstructure is observed for copper (5), whereas iron, cobalt, and manganese oxides exhibit a commensurate structure (3, 4).

The origin of these complex structural phenomena is so far not fully understood since several factors may act upon the modulation such as the cationic composition and the oxygen stoichiometry. Nevertheless, there is no doubt that the nature of the cations forming the distorted triple rock–salt layer "$SrBi_2O_3$" plays an important role in the appearance or disappearance of the modulation. The progressive substitution of lead for bismuth in those layers induces a variation of the modulation periodicity, up to the disappearance of this phenomena for higher contents (Bi/Pb ≈ 1) (7, 8). Such an evolution suggests that the $6s^2$ lone pair of Bi^{3+} is the primary cause of the distortion of the rock–salt-type layers due to steric effects, the larger size of Pb^{2+} being much less stereoactive than Bi^{3+} (9). Nevertheless, the presence of excess oxygen in the layer may also play a role, but it is not known whether it is a cause for this distortion or a consequence of the presence of lone-pair cations. Another important issue concerns the possibility to stabilize such triple rock–salt-type layers, in the absence of double-bismuth (or lead) layers. For this reason we have revisited the system Bi–Sr–Co–O, considering the Sr-rich compositions. We report, herein, for the first time the possibility to generate a nonmodulated 2201-type structure with a mixed $[(Bi_{0.5}Sr_{0.5}O)_2]_\infty$ double layer, corresponding to the formulation $Bi_{1-x}Sr_{3+x}CoO_{6-\delta}$ ($x \approx 0.13$).

EXPERIMENTAL

The system Bi–Sr–Co–O was investigated according to the generic formula $Bi_{2-x}Sr_{2+x}CoO_{6\pm\delta}$, using Bi_2O_3, SrO, and Co_3O_4 as reactants. To avoid carbonate contamination, SrO oxide was initially prepared by decomposing SrO_2 or $Sr(OH)_2 \cdot 8H_2O$ at 1100°C and stored in a dry box. The samples were prepared by solid state reaction, thoroughly mixing appropriate amounts of starting oxides. This step was also performed in a dry box. Next, the mixtures were introduced in a sealed and evacuated silica tube, then heated up to a temperature close to 900°C, at 150°C h^{-1}, kept at this temperature for 24 h, and quenched to room temperature.

0022-4596/99 $30.00

The oxygen content was determined by chemical analysis using redox titration.

The electron diffraction (ED) studies were carried out using a JEOL 200CX microscope fitted with an eucentric goniometer ($\pm 60^\circ$), while the high-resolution electron microscopy (HREM) was performed with a TOPCON 02B microscope operated at 200 kV and having a point resolution of 1.8 Å. HREM image calculations were carried out with the Mac-Tempas multislice program. Both microscopes are equipped with energy-dispersive spectroscopy (EDS) analyzers.

Powder X-ray diffraction patterns were collected using a Philips vertical diffractometer equipped with a secondary graphite monochromator and working with Cu$K\alpha$ radiation. Data were collected by step scanning over an angular range $5^\circ \leq 2\theta \leq 100^\circ$ and next were treated by profile analysis with the program Fullprof (version 3.2) (10).

The T-dependent susceptibility was measured with a Faraday balance (3 kG) for the high-temperature region (300 K $\leq T \leq$ 800 K) whereas the susceptibility was deduced from magnetization measurements collected with a Quantum Design SQUID magnetometer (5 K $\leq T \leq$ 400 K) under the same applied field of 3 kG. ac-susceptibility was also measured in a small H_{ac} magnetic field of 10 Oe with a Lake Shore susceptometer. Resistance measurements were performed with a four-probe technique for which four indium contacts were ultrasonically deposited on the top surface of the bar.

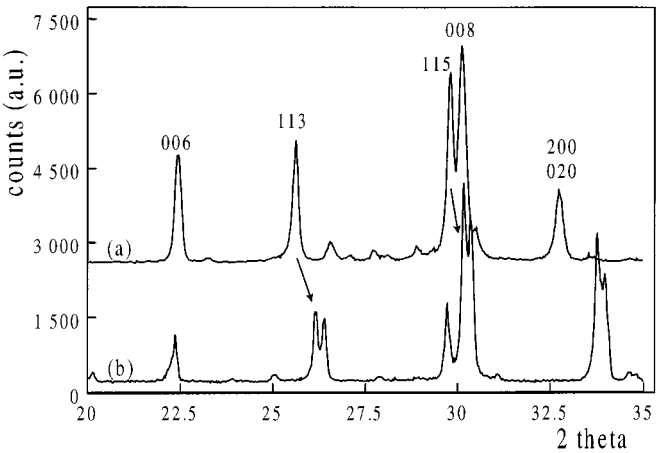

FIG. 1. Experimental X-ray patterns, $20^\circ \leq 2\theta \leq 35^\circ$, recorded for (a) $Bi_2Sr_2CoO_{6+\delta}$ and (b) $Bi_{0.82}Sr_{3.13}CoO_{6-\delta}$, showing the splitting of the (113) and (115) diffraction peaks.

RESULTS AND DISCUSSION

For the above experimental conditions, we confirm the existence of a 2201-type structure for the nominal composition $Bi_2Sr_2CoO_{6+\delta}$ (3). More importantly, a closely related structure is obtained for the nominal composition $BiSr_3CoO_6$. The comparison of the X-ray powder diffraction (XRPD) pattern of $Bi_2Sr_2CoO_{6+\delta}$ (Fig. 1a) and $BiSr_3CoO_6$ (Fig. 1b) shows that both oxides exhibit the 2201-type structure, but that the latter phase differs from the first by splitting of some fundamental reflections. This observation suggests a new lattice associated with a major structural modification with respect to $Bi_2Sr_2CoO_{6+\delta}$.

1. Basic Structure

Parallel to these preliminary XRPD investigations, coupled electron diffraction–EDS analyses have been performed on the strontium-rich sample (nominal $x = 1$). The average composition was determined from the analysis of more than 15 microcrystals: the actual cationic composition "$Bi_{0.82}Sr_{3.13}Co$" is close to the nominal one. CoO is observed as secondary phase (estimated to a few percent).

The reconstruction of the reciprocal space was carried out by tilting around the crystallographic axes. The set of intense reflections confirm the close relationships with the 2201-type structure, but the presence of additional reflections shows that complex structural features take place in this 2201-related structure and evidences a double cell with $a \approx b \approx a_p\sqrt{2}$ and $c \approx 24$ Å $\approx c_{2201}$. The only condition limiting the $0kl$ reflections is $00l$: $l = 2n$ (Fig. 2a). In contrast, the $h0l$ intense reflections form a centered rectangle (Fig. 2b), suggesting the presence of a n-type mirror. However, weak extra spots and diffuse streaks are systematically observed along c^* (see white arrows in Fig. 2b), which violate these conditions and suggest order–disorder phenomena. Similarly, very weak diffraction spots in the [001] ED patterns (Fig. 2c) show that there is no condition limiting the $hk0$ reflections. A slight monoclinic distortion is systematically detected, which is in agreement with the splitting of the (113) and (115) diffraction peaks ($2\theta \approx 26.3^\circ$ and 30.2°, respectively), clearly observed in the XRPD pattern (see arrows in Fig. 1). On the basis of these observations, the $P2_1$ space group (with unique axis **c**) has been retained and the cell parameters refined to $a = 5.2723(2)$ Å, $b = 5.3026(2)$ Å, $c = 24.006(1)$ Å, and $\gamma = 90^\circ 59(1)$.

The comparison of these cell parameters with those reported in the case of stoichiometric 2201-type structures $Bi_2Sr_2CoO_{6+\delta}$ (3), $a = 5.459(5)$ Å, $b = 5.426(2)$ Å, and $c = 23.450(4)$ Å, shows an opposite evolution of the a and c parameters. The c parameter increases but a and b parameters decrease so that the cell volume decreases from 699 to 671 Å^3; this effect is in disagreement with the Sr^{2+} substitution for Bi^{3+}, considering the ionic radii, and suggests an important rearrangement of the cations within the $[AO]_\infty$ layers. The presence of oxygen vacancies, estimated to $\delta = 0.2$ per formula unit from chemical analysis, could also play a role due to its influence on the cobalt oxidation

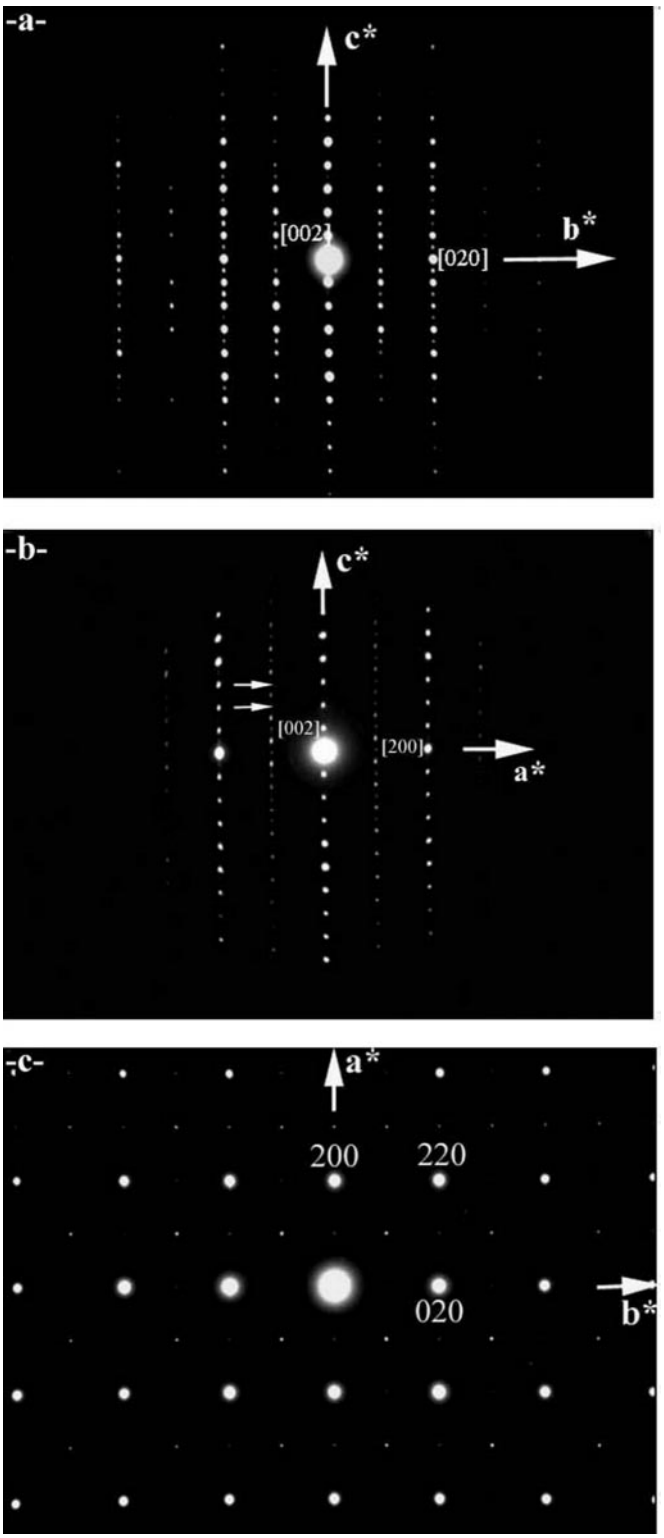

FIG. 2. Experimental ED patterns, oriented (a) [100], (b) [010], and (c) [001], indexed in the unit cell $a_p\sqrt{2} \times a_p\sqrt{2} \times c_{2201}$.

state. It should be noticed that such a drastic increase of the c parameter has already been observed in the system $Bi_{2-y}Pb_yBaLaCuO_{6+\delta}$ (11) which was associated with the

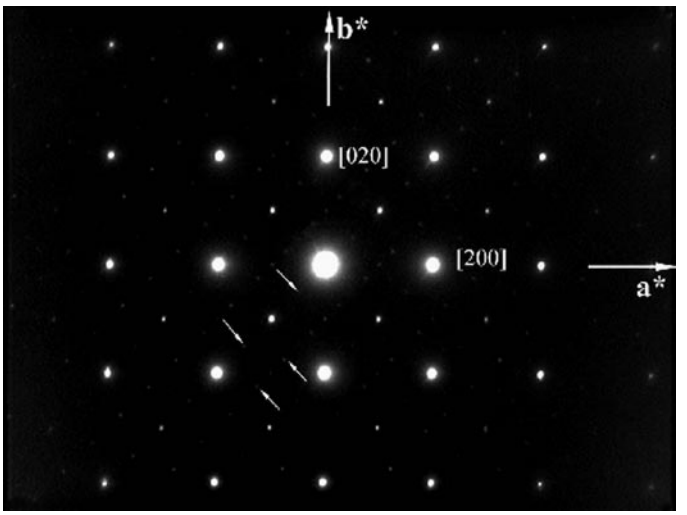

FIG. 3. Experimental ED patterns oriented [001] with the extra spots (white arrows) leading to a superstructure $4a_p \times 2a_p \times c_{2201}$.

disappearance of the modulation. Among the numerous crystallites characterized by ED, none exhibits the satellites usually associated with the $0k0$ Bragg reflections in the modulated structures. Thus, the $BiSr_3CoO_6$ 2201-type compound behaves similar to the Pb-substituted compounds $Bi_{2-x}Pb_xSr_2CoO_6$ (3, 12). Note, however, that very weak extra reflections (indicated by small arrows in Fig. 3) are often observed along [001] orientation, involving periodicities of $4a_p$ and $2a_p$ along the [110] and $[\bar{1}10]$ directions, respectively. The origins of the different additional reflections will be discussed further.

From the composition deduced from EDS analyses, namely, "$Bi_{0.82}Sr_{3.13}Co$," it appears that 1 bismuth atom out of 2 should be replaced by strontium, leading to mixed $[(Bi,Sr)O]_\infty$. Several models of distribution of these 2 cations within the 4 different layers can be considered, from long-range orderings, to a statistical distribution. To clarify the structure, especially to determine the existence and the localization of ordering phenomena and to understand the different phenomena responsible for the complex ED patterns, a HREM investigation was carried out.

The [110] and $[\bar{1}10]$ directions, i.e., the equivalent $[100]_p$ directions of the perovskite subcell, are the best for characterizing the nature of the layers stacked along **b**. They confirm that the stacking mode is that of the Bi-2201-type structure. This is illustrated in Fig. 4, where the high electronic density zones are highlighted. The four adjacent rows of staggered bright dots (arrows), 3.8 Å spaced along $[\bar{1}10]$ and 2.8 Å spaced along **c**, are characteristic of rock salt-type $[AO]_\infty$ layers. These groups are separated along **c**, with one row of gray dots associated with one $[CoO_2]_\infty$ layer. The sequence of four $[AO]_\infty$ layers alternating with one $[CoO_2]_\infty$ layer is highly regular.

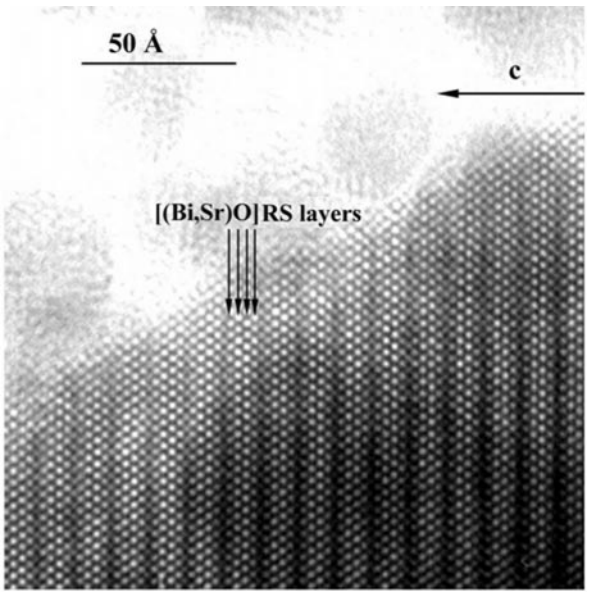

FIG. 4. Experimental HREM image recorded along to the [110] direction. Bright dots are correlated to Bi and Sr atoms.

[010] and [100] HREM images, recorded for focus values close to the above (bismuth and the strontium positions are correlated with the brighter dots) are displayed in Figs. 5a and 5b, respectively. The [010] images are also very close to those commonly observed along **b** in the 2201-type compounds. The Sr and Bi atoms form four rows of aligned bright dots, 2.65 Å spaced along **a**. At the level of the intermediate "bismuth double layers," a contrast variation is observed, forming sticks with a periodicity corresponding to a d value of 5.3 Å. These sticks (white arrows) are translated by $a/2$ in the adjacent groups of four rock–salt layers. This is, in fact, a feature commonly observed in the 2201- and 2212-type Bi–Sr–M–O (M = Cu, Mn, Co) oxides, which was correlated with the orientation of the cell (the modulation is perpendicular to the **a** axis) and the lowering of symmetry (loss of the ideal F-type lattice).

The [100] HREM images (Fig. 5b) display more information about the structure of the present phase. The first interesting point is that the $[(Bi,Sr)O]_\infty$ layers are flat, confirming the ED results which suggest a nonmodulated structure. Along **b**, the periodic (5.3 Å) contrast variation at the level of two intermediate $[AO]_\infty$ layers, with the alternation of one gray dot and one bright dot, is translated by $b/2$ in the adjacent layer (see black arrows) so that the double $[(Bi,Sr)O]_\infty$ layers appear as two rows of staggered bright dots. This contrast variation, associated with the actual cation content, "$Bi_{0.82}Sr_{3.13}Co$," suggests a 1:1-type ordering phenomenon at the level of the double $[(Bi,Sr)O]_\infty$ layers.

Although deviations from perfect ordering have been detected, as further detailed below, an ideal structural model can be proposed, taking into consideration these details. It corresponds to the formulation $BiSr_3CoO_6$ (Fig. 6), with an ordered and nonmodulated 2201-type structure, and the stacking of the different layers along **c** corresponding to the sequence "$[CoO_2]_\infty[SrO]_\infty[Bi_{0.5}Sr_{0.5}O]_\infty[Bi_{0.5}Sr_{0.5}O]_\infty[SrO]_\infty$."

2. *Structure Calculations*

To check the above model, structural calculations were performed using X-ray diffraction data, in the $P2_1$ space group (with unique **c** axis). This space group involves 22

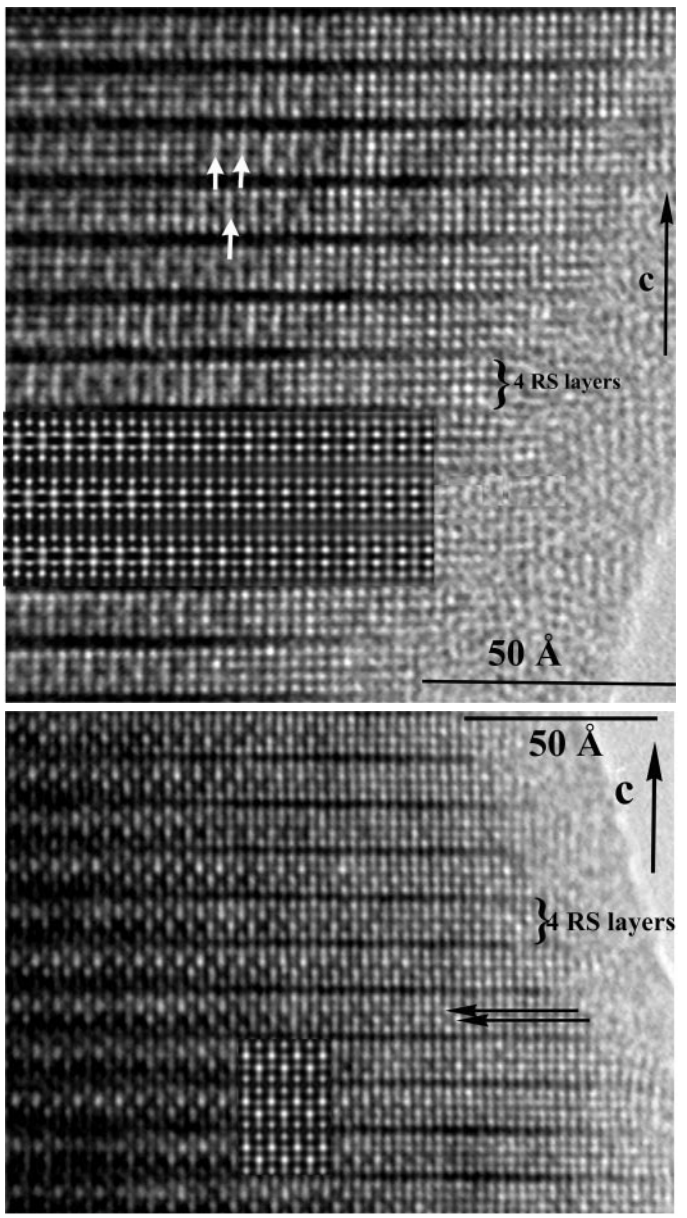

FIG. 5. Experimental HREM images recorded along (a) [010] and (b) [100] directions. Bright dots are correlated to Bi and Sr atoms.

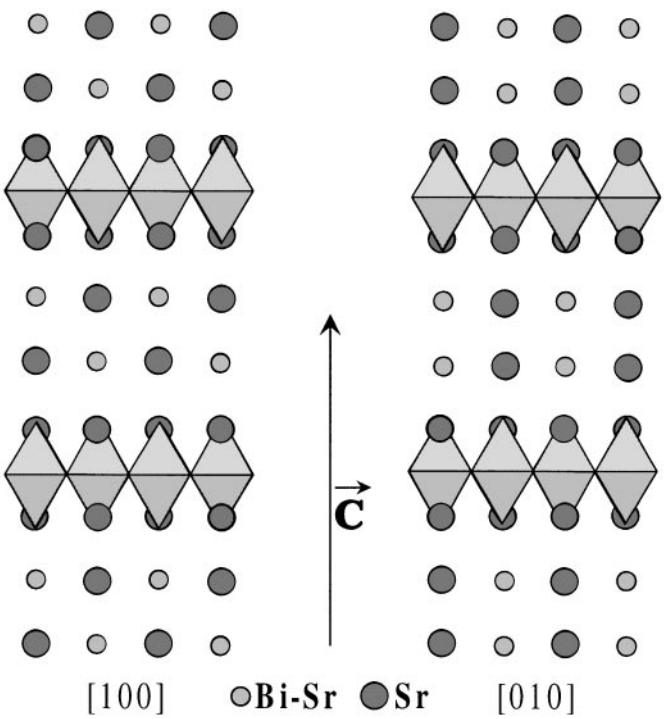

FIG. 6. Schematic drawing of the Bi–Sr ideal ordering shown along [100] and [010] directions. For simplicity, oxygen in the (Bi–Sr)O layers are not drawn.

independent atoms in the unique 2*a* site (*x*, *y*, *z*) to describe the 2201 type structure. For this reason and to avoid a large number of variable parameters, *x* and *y* variables were fixed to their theoretical value and were only refined if it appeared necessary during the calculations. In the same way, some positional parameters of the oxygen atoms were constrained to have similar displacements (see Table 1), and an overall isotropic *B* factor was applied for each kind of atom. All crystallographic sites were first assumed to be fully occupied for the calculations.

Refinement of the variable positional parameters for metallic and oxygen atoms, and then of isotropic *B* factors, quickly converged, giving for the agreement factors $R_p = 0.10$, $R_{wp} = 0.13$, $R_i = 0.085$, and $\chi^2 = 2.30$, but with rather high *B* values for oxygen atoms (4.65 Å^2). Analysis of the results showed that, at this step, it was necessary to displace O(9), O(10), O(11), and O(12) in the *ab* plane. Refinement of the new variables provided a decrease in R_i (0.076) and *B* for oxygen atoms (1.3 Å^2). At this stage oxygen deficiency was envisaged according to the chemical analysis which led to an oxygen content close to 5.8 per formula unit of $Bi_{0.82}Sr_{3.13}CoO_{5.8}$, i.e., +2.9 as the mean oxidation state of cobalt atoms assuming Bi(III) and Sr(II), respectively. Intermediate calculations of occupancy factors of oxygen sites showed without ambiguity that only 2 sites out of 12, O(1) and O(3), are possibly deficient. Oxygen vacancies were then equally distributed over the 2 sites with a value deduced from the chemical analysis and were not refined. The final agreement factors, $R_p = 0.096$, $R_{wp} = 0.125$, $R_i = 0.073$, and $\chi^2 = 2.16$, were obtained for the refined structural parameters listed in Table 1. The calculated and difference X-ray powder diffraction patterns are plotted in Fig. 7. The weight percentage of the secondary phase was found to be 1.9%.

These results show that the structural model established from the HREM images is correct.

3. *Description of the Structure*

Perspective views of the structure are given in Fig. 8. The structure of this cobaltite can be described, like the stoichiometric Bi-2201 structure, as the intergrowth of distorted perovskite layers with triple rock salt-type $[BiSr_2O_3]_\infty$ layers (Fig. 8a). However, even if XRPD cannot display accurate values for O positions, the calculated interatomic Co–O distances (Table 2) clearly show that the cobalt layer is better described by two sorts of CoO_x polyhedra: dissymmetrically elongated Co(1) octahedra and slightly flattened Co(2) tetragonal pyramids. Consequently,

TABLE 1

Refined Variable Structural Parameters for $BiSr_3CoO_{5.8}$ (Space Group, $P2_1$; Lattice Constants, $a = 5.2723(6)$ Å, $b = 5.3026(6)$ Å, $c = 24.006(3)$ Å, and $\beta = 90.59^\circ$ (1)

Atom	*x*	*y*	*z*	*B* (Å^2)	*n*
Bi(1)	0.75[a]	0.5[a]	0.5614(26)	0.20(5)[b]	2
Bi(2)	0.75[a]	0.0[a]	0.4438(26)	0.20(5)[b]	2
Sr(1)	0.25[a]	0.5[a]	0.3333(27)	0.63(8)[c]	2
Sr(2)	0.25[a]	0.0[a]	0.6788(27)	0.63(8)[c]	2
Sr(3)	0.25[a]	0.5[a]	0.1751(27)	0.63(8)[c]	2
Sr(4)	0.25[a]	0.0[a]	0.8343(27)	0.63(8)[c]	2
Sr(5)	0.25[a]	0.0[a]	0.4469(32)	0.63(8)[c]	2
Sr(6)	0.25[a]	0.5[a]	0.5595(32)	0.63(8)[c]	2
Co(1)	0.25[a]	0.0[a]	0.2506(28)	0.7(3)[d]	2
Co(2)	0.25[a]	0.5[a]	0.7351(27)	0.7(3)[d]	2
O(1)	0.0[a]	0.25[a]	0.25[a]	0.3(3)[e]	1.6
O(2)	0.5[a]	0.25[a]	0.25[a]	0.3(3)[e]	2
O(3)	0.0[a]	0.75[a]	0.25[a]	0.3(3)[e]	1.6
O(4)	0.5[a]	0.75[a]	0.25[a]	0.3(3)[e]	2
O(5)	0.25[a]	0.0[a]	0.3438(12)	0.3(3)[e]	2
O(6)	0.25[a]	0.5[a]	0.6582(12)	0.3(3)[e]	2
O(7)	0.25[a]	0.0[a]	0.1483(12)	0.3(3)[e]	2
O(8)	0.25[a]	0.5[a]	0.8517(12)	0.3(3)[e]	2
O(9)	0.366(6)	0.574(8)	0.4379(18)	0.3(3)[e]	2
O(10)	0.134(6)	0.074(8)	0.5621(18)	0.3(3)[e]	2
O(11)	0.795(9)	−0.078(7)	0.4428(16)	0.3(3)[e]	2
O(12)	0.705(9)	0.578(7)	0.5572(16)	0.3(3)[e]	2

Note. Constraints for oxygen atoms: $x_{O(9)} + x_{O(10)} = 0.5$; $x_{O(11)} + x_{O(12)} = 1.5$; $y_{O(9)} - y_{O(10)} = 0.5$; $y_{O(11)} + y_{O(12)} = 0.5$; and for $i = 5, 7, 9, 11$, $z_{O(i)} + z_{O(i+1)} = 1$.

[a] Not refined parameters.

[b–e] Parameters constrained to have the same value.

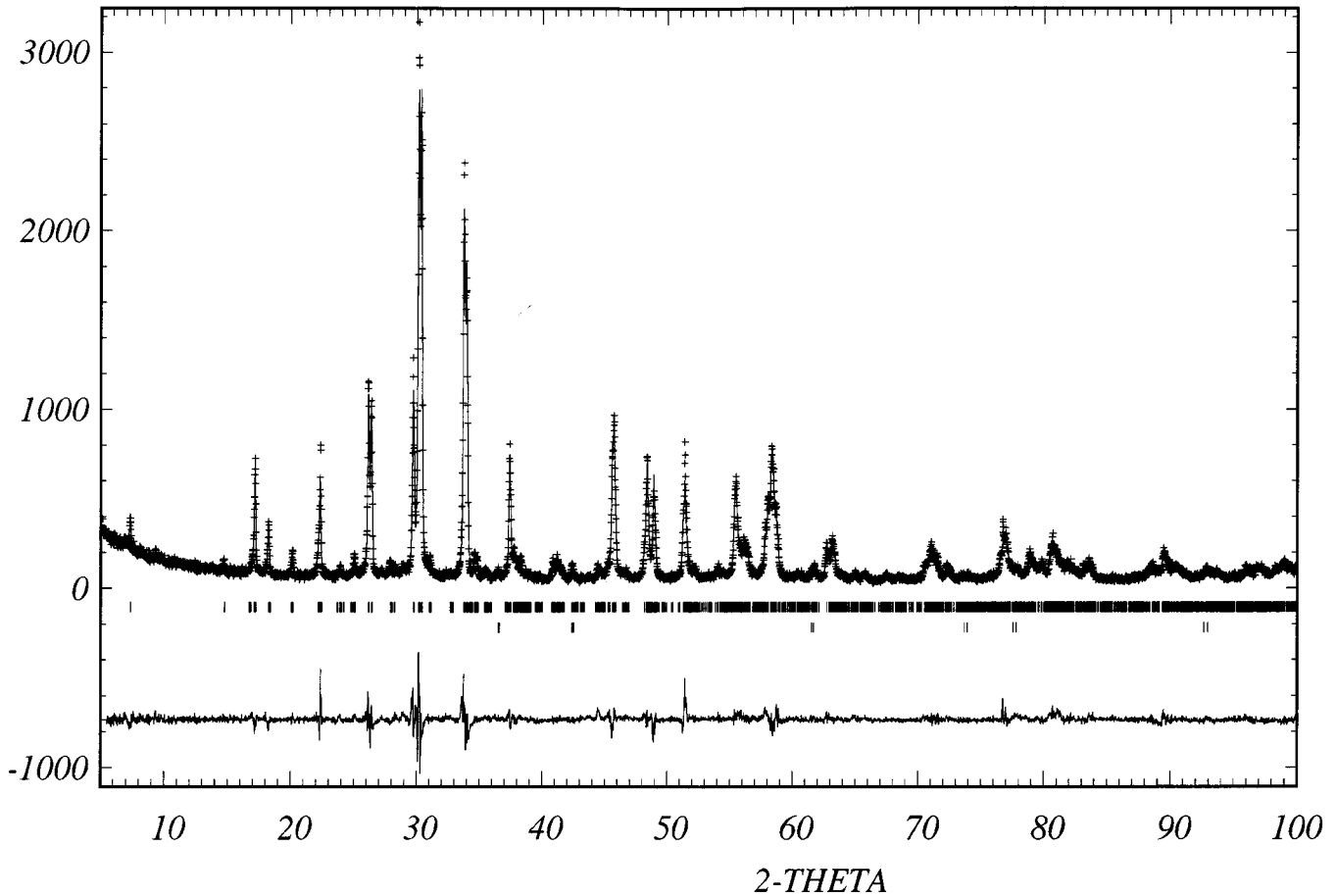

FIG. 7. Experimental (crosses) and calculated and difference (solid lines) powder X-ray diffraction patterns of the 2201-type phase $Bi_{0.82}Sr_{3.13}CoO_{5.8}$. Verticals bars indicate the Bragg angle positions for the main phase (upper) and the impurity CoO (lower).

the cobalt layer consists of rows of CoO_6 octahedra (Co(1)) and of CoO_5 pyramids (Co(2)) running along **b** and stacked along **a** alternately by sharing their equatorial apices (Fig. 8b). As a result, one Co(1) octahedron alternates with one Co(2) pyramid along [110] or [$\bar{1}$10].

The important difference with respect to the classical Bi-2201 structure concerns the replacement of the two $[BiO]_\infty$ layers by two $[Bi_{0.5}Sr_{0.5}O]_\infty$ layers in which one bismuth atom alternates with one strontium atom along **a**. It results in the formation of double $(BiO)_2$ ribbons running along **b** and parallel to (100) (Fig. 9a); these ribbons are stacked along **a** in such a way that one double $(BiO)_2$ ribbon alternates with one double $(SrO)_2$ ribbon (Fig. 8a).

This arrangement of the BiO chains exhibits a similarity with that observed in the tubular-2 phases $Bi_{3.6}Sr_{12.4}Mn_8O_{28+\delta}$ (13) and $Bi_{3.7}Sr_{11.4}Co_8O_{28-\delta}$ (14). For those oxides, one also observes double $(BiO)_2$ ribbons, running along **a**, sandwiched between SrO chains (Fig. 9b). More importantly, it is remarkable that each Bi^{3+} cation has three nearest neighbors, forming approximately 90° oriented Bi–O bonds, ranging from 2.06 to 2.25 Å (Table 2). This geometry is very similar to that encountered in the tubular-2 phases (13, 14), so that the coordination of bismuth can be described, as distorted tetrahedral, BiO_3L, taking into consideration the stereoactivity of its $6s^2$ lone pair denoted L (see Fig. 9). Note also that the Bi–O apical bond along **c** weakens noticeably the Co–O apical bond of the Co polyhedra: it is opposed to the longest Co–O bond in the Co(1) octahedra (2.45 Å) and leads to an apical Co(2)–O bond of 2.79 Å, so that the Co(2) polyhedron is better described as a pyramid rather than an octahedron. The Sr–O distances (Table 2), significantly larger than the Bi–O ones, are in agreement with the ordering of Bi^{3+} and Sr^{2+}.

The nonstoichiometry phenomena that appear in this oxide are rather complex. Concerning the cations, a bismuth deficiency and an excess strontium have been observed by EDS analysis, with regard to the ideal formula $BiSr_3CoO_x$. This implies that some Bi sites are partially occupied by strontium (about 10%). This deviation from stoichiometry

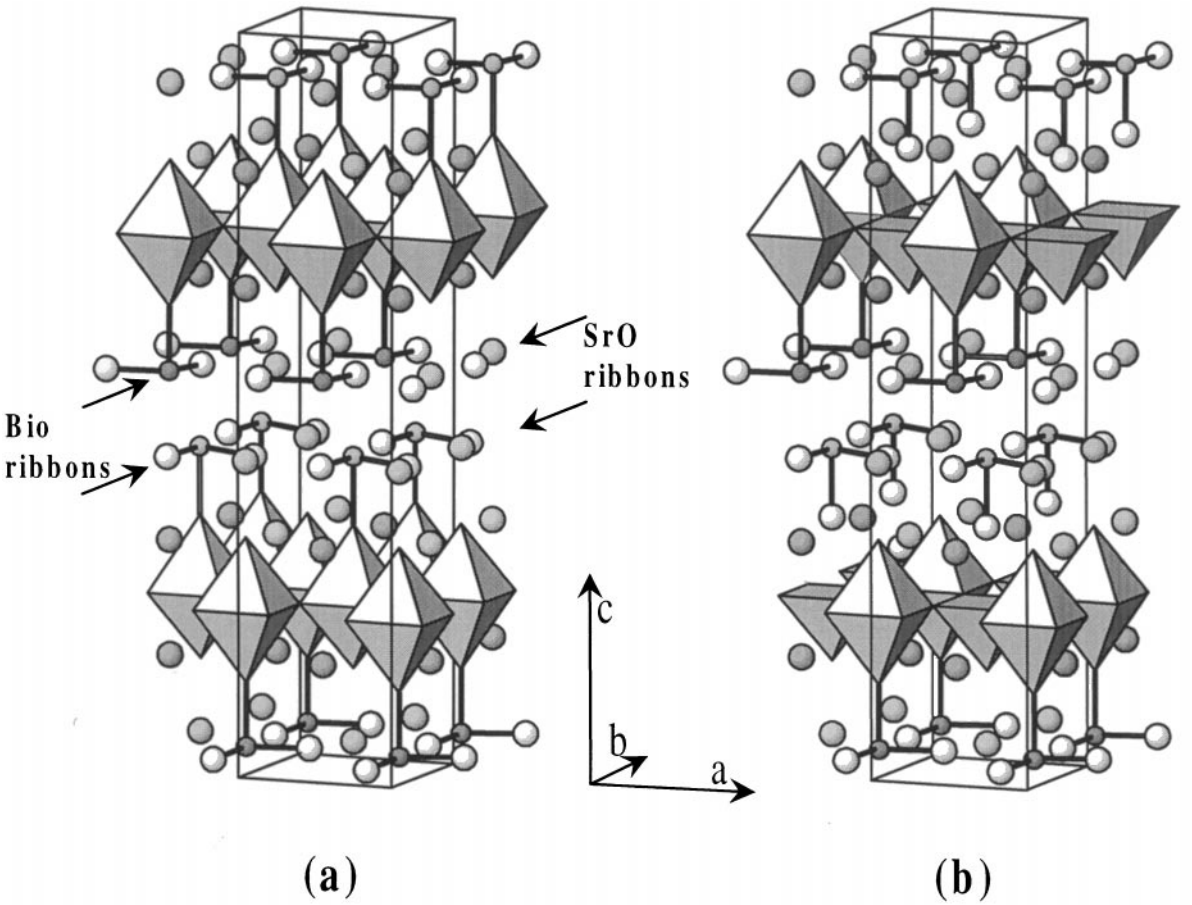

FIG. 8. Perspective view of the structure drawn for the ideal composition $BiSr_3CoO_6$ showing the three Bi–O bonds. In (a) the cobalt environment is considered as octahedral whereas in (b) it is assumed half-octahedral and half-square-pyramidal due to the very long Co(2)–O(8) distance.

($Bi_{0.82}Sr_{3.13}CoO_x$ instead of $BiSr_3CoO_x$) was not considered in our calculations, due to the excessive number of parameters that are involved. The oxygen deficiency, on the O(1) and O(3) sites, is also significant, and oxygen vacancy ordering may also be responsible for superstructures often observed in ED patterns. Note, however, that the creation of one oxygen vacancy on the O(1) or O(3) site leads to the formation of one Co(1) pyramid and one Co(2) distorted tetrahedron simultaneously, so that a local rearrangement of the surrounding oxygen may be involved, which cannot be determined in the present study.

4. Microstructure: Twinning Phenomena and Oxygen Non stoichiometry Effects

Simulated HREM images were calculated using the positional parameters refined from XRPD data. The comparison of experimental and simulated HREM images (inset of Figs. 5a and 5b) confirms the 2201-type structure and shows that the 1:1 ordering of Bi^{3+} and Sr^{2+} species within the distorted rock salt-type layers generates the contrast variations observed along the different directions in the experimental images. Such a good fit allowed us to understand the origin of the extra reflections and diffuse streaks observed in the ED patterns.

Microtwinning. The extra weak spots or diffuse streaks observed along **c***, especially in the [100] and [010] ED patterns (Figs. 2a and 2b), are generated by microtwinning phenomena. They result from the stacking of [100] and [010] oriented domains along **c**. These twinning domains are generated by the fact that the ordering phenomenon takes place along one or the other of the two equivalent directions of the tetragonal 2201 subcell. In the images, they are easily detected (Fig. 10) by the complex combination of the two types of contrast, sticks or staggered dots (see white arrows in Fig. 10), which are characteristic of the [010] and [100] orientations, respectively.

This phenomenon is also visible along [110] and [$\bar{1}$10], which exhibit different contrasts due to the monoclinic

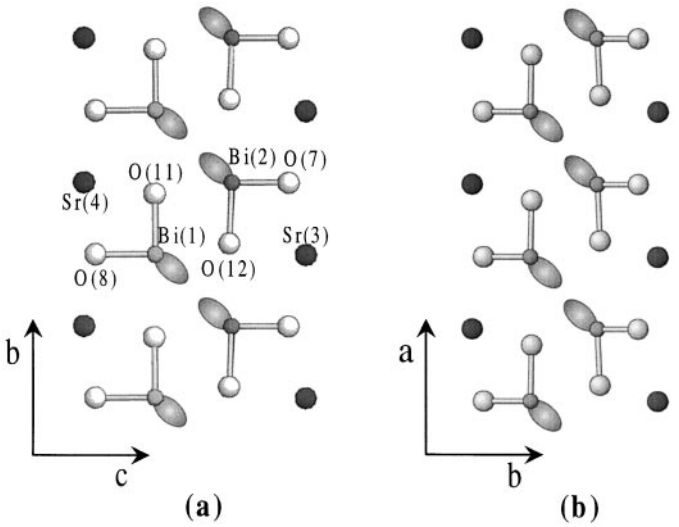

FIG. 9. Projections of the Bi–O ribbons in $Bi_{0.82}Sr_{3.13}CoO_{5.8}$ (a) and the tubular two phases (b). The possible orientations of the $6s^2$ lone pair (L) of Bi^{3+} are shown, leading to the formation of distorted BiO_3L tetrahedra (the third oxygen atoms which are out of plane are not drawn).

distortion. This is illustrated in Fig. 11 where, for a focus value close to -250 Å, the cation positions are imaged as dark dots at the thin edge of the crystal. In the thicker part, two types of different contrasts are observed at the level of the $[(Bi_{0.5}Sr_{0.5})O]_\infty$ bilayers (white arrows): a double row of staggered bright dots for the [110] orientation of the domains and a single row of elongated dots for the $[\bar{1}10]$ orientation. This image presents an interesting phenomenon, rather commonly observed, which consists of a regular twinning with very short periodicities. This effect corresponds to a so-called chemical twinning and involves a new local stacking mode associated with the formation of a complex supercell. The basic superstructure, corresponding to an ideal tetragonal cell $a_I = a \approx 5.3$ Å and $c_I = c_{2201} \approx 24$ Å, is built up from alternating [110] and $[\bar{1}10]$ domains which are 12 Å thick with a translation of $c/2$ of the ordered $[(Bi_{0.5}Sr_{0.5})O]_\infty$ bilayer (Fig. 12).

Oxygen nonstoichiometry. The X-ray refinements establish, in agreement with the chemical analysis, an oxygen deficiency of the $Bi_{0.82}Sr_{3.13}CoO_{5.8}$ sample, with the oxygen vacancies being located in the $[CoO_{2-\delta}]_\infty$ layers (see Table 1). To determine how the oxygen stoichiometry plays a role on the cell parameters, especially on the monoclinic distortion, a complementary study was carried out on the same sample. After oxygen pressure annealing (100 bar, 450°C) the chemical analysis shows an actual stoichiometry close to 6 per unit formula and the cell parameters, refined from XRPD data, converge toward a pseudo-orthorhombic lattice: $a = 5.3034(8)$ Å, $b = 5.3285(7)$ Å, $c = 23.750(3)$ Å, and $\gamma = 90°37(1)$.

From the ED investigation, the original and annealed samples mainly differ by the presence or absence, respectively, of a set of additional reflections. These satellites, mentioned in the first section, are especially observed in the [001] ED patterns of the original samples (Fig. 3) and involve the periodicities $a_{II} \approx 4a_p$ and $b_{II} \approx 2a_p$ along [110] and $[\bar{1}10]$. In the [110] and $[\bar{1}10]$ ED patterns, these satellites are quite invisible and the corresponding images show that they are associated with only local contrast variations. This is illustrated in Fig. 13 where a modulated contrast (see white arrow) with a local periodicity of $4a$, is observed at the level of oxygen positions belonging to $[CoO_2]_\infty$ layers, suggesting a local ordering of oxygen atoms and oxygen vacancies. In the annealed sample, these satellites are no longer observed, supporting the hypothesis that they are correlated to the oxygen deficiency.

It is important to note that all these phenomena which generate extra reflections and diffuse streaks in the ED patterns are only correlated to order–disorder phenomena

TABLE 2
Interatomic Distances

Distances (Å)			Distances (Å)		
Co(1)–O(1)	×1	1.879(1)	Co(2)–O(1)	×1	1.91(1)
Co(1)–O(2)	×1	1.860(1)	Co(2)–O(2)	×1	1.89(1)
Co(1)–O(3)	×1	1.860(1)	Co(2)–O(3)	×1	1.89(1)
Co(1)–O(4)	×1	1.879(1)	Co(2)–O(4)	×1	1.91(1)
Co(1)–O(5)	×1	2.24(7)	Co(2)–O(6)	×1	1.89(7)
Co(1)–O(7)	×1	2.45(7)	Co(2)–O(8)	×1	2.79(7)
Bi(1)–O(7)	×1	2.09(7)	Bi(2)–O(8)	×1	2.21(7)
Bi(1)–O(10)	×1	2.06(3)	Bi(2)–O(9)	×1	2.07(3)
Bi(1)–O(11)	×1	2.89(7)	Bi(2)–O(11)	×1	3.08(4)
Bi(1)–O(12)	×1	2.25(4)	Bi(2)–O(11)	×1	2.25(4)
Bi(1)–O(12)	×1	3.08(4)	Bi(2)–O(12)	×1	2.76(7)
Sr(1)–O(1)	×1	2.73(5)	Sr(2)–O(1)	×1	2.53(4)
Sr(1)–O(2)	×1	2.74(5)	Sr(2)–O(2)	×1	2.54(4)
Sr(1)–O(3)	×1	2.74(5)	Sr(2)–O(3)	×1	2.54(4)
Sr(1)–O(4)	×1	2.73(5)	Sr(2)–O(4)	×1	2.53(4)
Sr(1)–O(5)	×1	2.66(1)	Sr(2)–O(6)	×2	2.71(1)
Sr(1)–O(8)	×2	2.67(1)	Sr(2)–O(7)	×2	2.74(2)
Sr(1)–O(9)	×1	2.61(7)	Sr(2)–O(10)	×1	2.89(7)
Sr(3)–O(1)	×1	2.59(4)	Sr(4)–O(1)	×1	2.75(5)
Sr(3)–O(2)	×1	2.60(4)	Sr(4)–O(2)	×1	2.76(5)
Sr(3)–O(3)	×1	2.60(4)	Sr(4)–O(3)	×1	2.76(5)
Sr(3)–O(4)	×1	2.59(4)	Sr(4)–O(4)	×1	2.75(5)
Sr(3)–O(6)	×2	2.67(1)	Sr(4)–O(5)	×2	2.65(1)
Sr(3)–O(7)	×2	2.73(2)	Sr(4)–O(8)	×2	2.68(1)
Sr(3)–O(12)	×1	2.87(7)	Sr(4)–O(11)	×1	2.65(7)
Sr(5)–O(5)	×1	2.47(8)	Sr(6)–O(6)	×1	2.32(8)
Sr(5)–O(9)	×1	2.36(4)	Sr(6)–O(9)	×1	3.01(8)
Sr(5)–O(9)	×1	3.10(4)	Sr(6)–O(10)	×1	2.34(4)
Sr(5)–O(10)	×1	2.86(8)	Sr(6)–O(10)	×1	3.11(4)
Sr(5)–O(11)	×1	2.43(5)	Sr(6)–O(12)	×1	2.91(5)
Sr(5)–O(11)	×1	2.91(7)	Sr(6)–O(12)	×1	2.43(5)

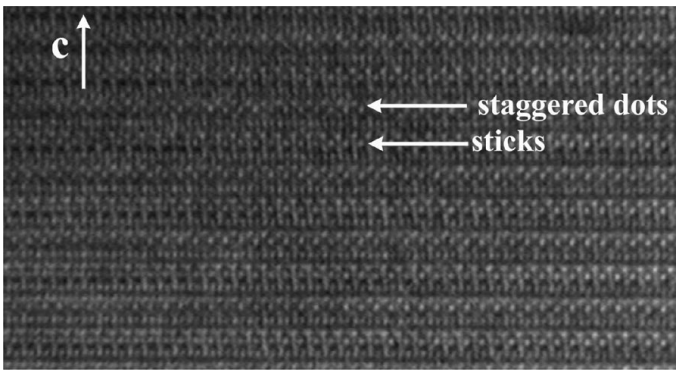

FIG. 10. Experimental HREM image showing the stacking along **c** of the [100] and [010] oriented domains.

between Bi/Sr at the level of the intermediate mixed $[(Bi_{0.5}Sr_{0.5})O]_\infty$ layers and O/□ at the level of the $[CoO_2]_\infty$ layers. They never involve important deviations from the ideal ordered structure.

5. *Physical Properties*

The resistivity measurements show that this 2201-type cobaltite is semiconducting with a ρ value of $\approx 100\ \Omega$-cm at 400 K for the as-prepared ceramic. This value is close to that reported for the $Bi_{3.7}Sr_{11.4}Co_8O_{28-\delta}$ cobaltite (14).

The temperature dependence of the molar magnetic susceptibility is plotted in Fig. 14. The Curie–Weiss fitting of the $\chi_M^{-1}(T)$ curve for the high-temperature range (300–600 K), with the formula $\chi = \chi_0 + C/(T - \theta_p)$ values, where C and θ_p are the Curie constant and the paramagnetic Curie temperature, respectively, and χ_0 is a T-independent

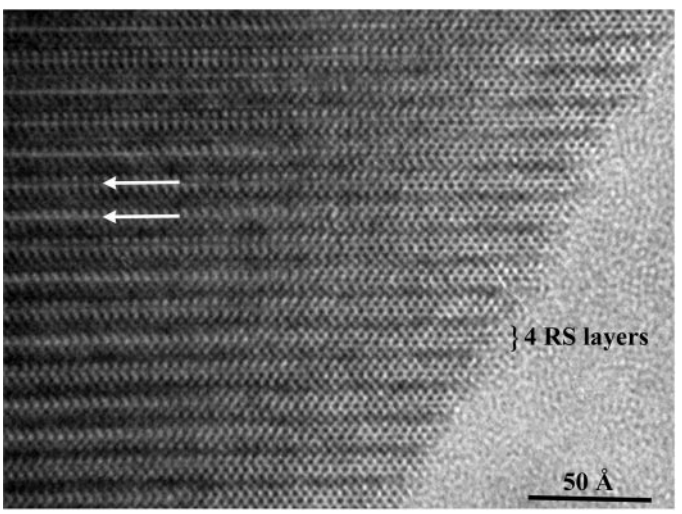

FIG. 11. Experimental HREM image recorded along [110]-type orientation showing microtwinning phenomena (white arrows). Dark dots in the thin edge of the crystal are correlated to Bi and Sr atoms.

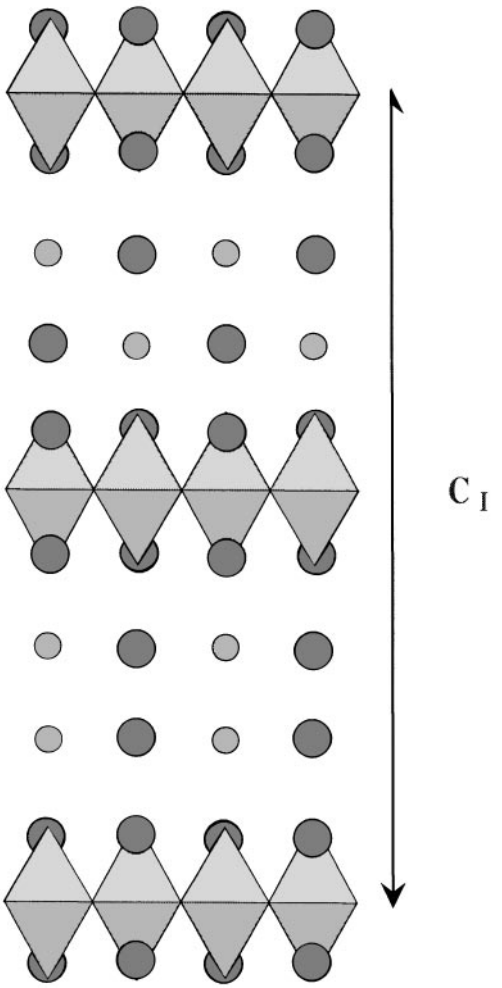

FIG. 12. Schematic drawing of the stacking mode in a new lattice labeled 1, corresponding to the 90° rotation of the BiO and SrO ribbons (the oxygen of these ribbons are not shown). The atom labels are the same as those in Fig. 6.

susceptibility term that leads to $\theta_p = -98$ K, indicating antiferromagnetic interactions. An effective paramagnetic moment close to 3.8 μ_B is obtained which cannot be simply related to the cobalt valence of 2.9 deduced from the chemical formula proposed in the structural part. This result suggests that the spin state of this essentially trivalent cobalt is not purely high spin (expected $\mu_{eff} = 5.4\ \mu_B$). A similar disagreement between μ_{eff} and expected values has already been reported for the two-dimensional (2D) $Bi_2Sr_2CoO_6$ oxide (3).

The low-temperature part of the $\chi_M^{-1}(T)$ curve shows that the curve deviates downward from the linear paramagnetic regime below 250 K (inset Fig. 14). This soft transition, suggesting the existence of weak ferromagnetic interactions, is then followed by a dramatic drop of χ below 50 K as shown from the $\chi_M(T)$ curve. A similar antiferromagnetic

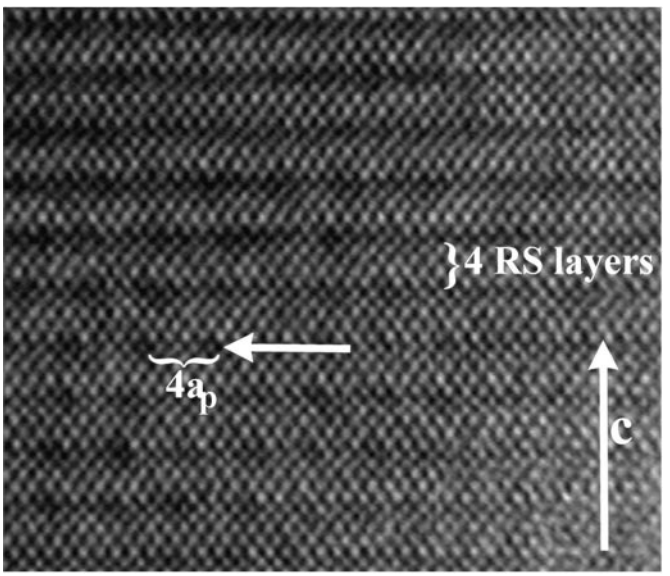

FIG. 13. Experimental [110] HREM image showing a local contrast variations at the level of $[CoO_2]_\infty$ layers (white arrow) with a periodicity of $4a_p$.

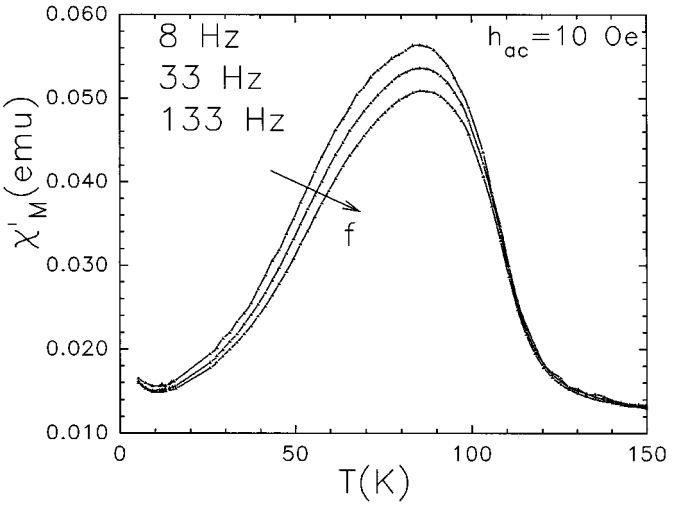

FIG. 15. Real part of the ac–χ versus T for $Bi_{0.82}Sr_{1.13}CoO_{5.8}$. The frequencies are labeled in the graph.

transition was also observed for the $Bi_{3.7}Sr_{11.4}Co_8O_{28-\delta}$ tubular cobaltite (14). Such a large decrease of χ may be attributed to a Co spin-state modification at low temperature toward a lower spin state. The coexistence of ferromagnetic and antiferromagnetic interactions should, in principle, induce some relaxation phenomena. This is clearly visible in Fig. 15 which shows the ac–χ' curves registered for three frequencies. The clear separation of the three corresponding curves, occurring below 105 K, confirms the existence of relaxation phenomena in this 2D oxide.

The magnetic structure of this cobaltite must be studied by neutron diffraction to explain the magnetic properties of this new oxide. In particular, the possibility of a spin-state transition occurring below 50 K or the existence of a canted antiferromagnetic structure which would yield ferromagnetic interactions must be discriminated.

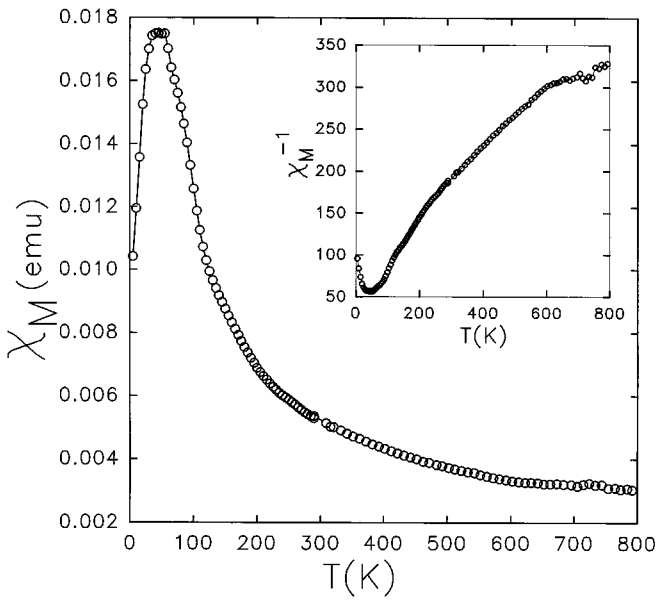

FIG. 14. Temperature dependence of the molar magnetic susceptibility. In insert $\chi_M^{-1} = f(T)$ is plotted.

CONCLUDING REMARKS

A 2201-type structure with a majority of strontium in the distorted triple-rock–salt layer has been synthesized for the first time. The first originality of the oxide $Bi_{1-x}Sr_{3+x}CoO_{6-\delta}$ concerns the absence of modulation. This point strongly supports the hypothesis according to which the $6s^2$ lone pair of Bi^{3+} is at the origin of the modulations in these compounds. It is also corroborated by the fact that the substitution of Bi^{3+} by Pb^{2+}, whose $6s^2$ lone pair is much less stereoactive, tends to dampen out the structure modulation. However, the solid solution $Bi_{2-x}Sr_{2+x}CoO_{6-\delta}$ will need a complementary study to clarify the unusual variation of cell parameters associated with the transition from modulated to nonmodulated structure.

The second important feature deals with the 1:1 ordering of Bi^{3+} and Sr^{2+} species along **a** within the double intermediate rock–salt layer. The existence of extended defects, corresponding to similar ordering of these cations but along two directions, **a** and **b**, suggests the possibility of generation of new 2201-type structures. The oxygen and cationic nonstoichiometry in this oxide, though clearly evidenced, is so far not understood and will require a neutron diffraction

study to clarify the magnetic behavior, especially, the antiferromagnetic transition at low temperature.

ACKNOWLEDGMENT

The authors are grateful to D. N. Nguyen for susceptibility measurements at high temperature.

REFERENCES

1. B. Raveau, C. Michel, M. Hervieu, and D. Groult, *in* "Crystal Chemistry of High Tc Superconductive Cuprates," Springer Verlag, New York, 1991.
2. J. M. Tarascon, W. R. McKinnon, and Y. Le Page, "Chemistry of high temperature superconductors" (C. N. R. Rao, Ed.), p. 186. World Scientific Publishing Corp., Singapore, 1991.
3. J. M. Tarascon, P. F. Miceli, P. Barboux, D. M. Hwang, G. W. Hull, M. Giroud, L. H. Greene, Y. Lepage, W. R. McKinnon, E. Tselepis, G. Pleizier, M. Eibschutz, D. A. Neumann, and J. J. Phyne, *Phys. Rev. B* **39,** 11587 (1989).
4. J. M. Tarascon, Y. Le Page, and W. R. McKinnon, *Eur. J. Solid State Chem.* **27,** 81 (1990).
5. C. Michel, M. Hervieu, M. M. Borel, A. Grandin, F. Deslandes, J. Provost, and B. Raveau, *Z. Phys. B* **68,** 421 (1987).
6. Y. Matsui, S. Takekawa, S. Horiuchi, and A. Umezono, *Jpn J. Appl. Phys.* **27,** 11873 (1988).
7. A. Maeda, Y. Kato, T. Shibauchi, Y. Nakajima, H. Watanabe, and K. Uchinokura, *Jpn J. Appl. Phys.* **28,** 1549 (1989).
8. J. M. Tarascon, Y. Le Page, W. R. McKinnon, R. Ramesh, M. Eibschutz, E. Tselepis, E. Wang, and G. W. Hull, *Physica C* **167,** 20 (1990).
9. J. Galy, G. Meunier, S. Anderson, and A. Aström, *J. Solid State Chem.* **13,** 142 (1975).
10. J. Rodriguez-Carvajal, *Physica B* **192,** 55 (1993).
11. A. Q. Pham, C. Michel, M. Hervieu, and B. Raveau, *J. Phys. Chem Solids* **54,** 65 (1993).
12. K. Yanagisawa, Y. Matsui, K. Shoda, E. Takayama-Muromachi, and S. Horiuchi, *Physica C* **196,** 34 (1992).
13. D. Pelloquin, C. Michel, A. Maignan, M. Hervieu, and B. Raveau, *J. Solid State Chem.* **138,** 278 (1998).
14. D. Pelloquin, A. C. Masset, A. Maignan, C. Michel, M. Hervieu, and B. Raveau, *Chem. Mater.* **11,** 84 (1999).